Published in final edited form as:
Adv Funct Mater. 2020 January 23; 30(4): . doi:10.1002/adfm.201906836.

Moldless Printing of Silicone Lenses With Embedded Nanostructured Optical Filters

Stefano Mariani[#], **Valentina Robbiano**[#], **Rossella Iglio**[#], **Antonino A. La Mattina**, **Pantea Nadimi**
Department of Information Engineering, University of Pisa, Via G. Caruso 16, 56122, Italy

Joanna Wang, **Byungji Kim**
Materials Science and Engineering Program, University of California, San Diego, 9500 Gilman Drive, La Jolla, California 92093, United States

Tushar Kumeria, **Michael J. Sailor**
Department of Chemistry and Biochemistry, University of California, San Diego, 9500 Gilman Drive, La Jolla, California 92093, United States

Giuseppe Barillaro
Department of Information Engineering, University of Pisa, Via G. Caruso 16, 56122, Italy

Abstract

Optical lenses are among the oldest technological innovations (3000 years ago) and they have enabled a multitude of applications in healthcare and in our daily lives. The primary function of optical lenses has changed little over time; they serve mainly as a light-collection (e.g. reflected, transmitted, diffracted) element, and the wavelength and/or intensity of the collected light is usually manipulated by coupling with various external optical filter elements or coatings. This generally results in losses associated with multiple interfacial reflections, and increases the complexity of design and construction.

In this work we introduce a change in this paradigm, by integrating both light-shaping and image magnification into a single lens element using a moldless procedure that takes advantage of the physical and optical properties of mesoporous silicon (PSi) photonic crystal nanostructures. Casting of a liquid poly(dimethyl) siloxane (PDMS) pre-polymer solution onto a PSi film generates a droplet with contact angle that is readily controlled by the silicon nanostructure, and adhesion of the cured polymer to the PSi photonic crystal allows preparation of lightweight (10 mg) freestanding lenses (4.7 mm focal length) with an embedded optical component (e.g. optical rugate filter, resonant cavity, distributed Bragg reflector). Our fabrication process shows excellent reliability (yield 95%) and low cost and we expect our lens to have implications in a wide range of applications. As a proof-of-concept, using a single monolithic lens/filter element we demonstrate: fluorescence imaging of isolated human cancer cells with rejection of the blue excitation light, through a lens that is self-adhered to a commercial smartphone; shaping the emission spectrum of

---

giuseppe.barillaro@unipi.it.
[#]These authors contributed equally

Supporting Information
Supporting Information is available from the Wiley Online Library or from the authors.

a white light emitting diode (LED) to tune the color from red through blue; and selection of a narrow wavelength band (bandwidth 5 nm) from a fluorescent molecular probe.

Graphical Abstract

Monolithic silicone lenses containing integral optical filters are prepared by casting of a liquid silicone pre-polymer solution onto a porous silicon photonic crystal, whose surface nanostructure has been engineered to form a near-perfect hemispherical lens. The self-adherent lenses can convert a smartphone camera into a high-fidelity fluorescence microscope without complicated fixturing.

Keywords

silicone micro lenses; nanostructured optical filters; porous silicon; fluorescence microscopy; cell imaging

Introduction

The earliest known lenses, made from polished crystal, were fabricated by the Assyrians in 700 BCE. One example is the Layard/Nimrud lens [1], which is thought to have been used either as an optical magnifier or as a means to start fires by concentrating sunlight. The earliest verified optical microscope was invented in the 13th century; it made use of a single lens magnifying glass and it provided relatively low magnification [2]. This time period also marks the beginning of the optics industry, which involved grinding and polishing lenses for use in spectacles. Galileo Galilei is sometimes cited as the inventor of the compound microscope/telescope [3], though Antonie van Leeuwenhoek (1595) is credited for its popularization by bringing the microscope to the attention of biologists [4]. In 1858 Joseph von Gerlach performed the first histological staining of brain tissue, using solutions of carmine dye to differentially stain and recognize the nucleus and nuclear granules.

Fluorescent compounds (e.g. synthetic fluorescein) and fluorescence microscopes appeared later, in 1871 and in 1911, respectively [5].

Three thousand years after its first appearance, commercial optical lenses are still prepared by either mechanical polishing or molding of rigid materials, such as glass [6] or plastics [7], and optical microscopes still rely on the use of lenses as a light collection element (for reflected, emitted, and/or diffracted light) and discrete optical filters for light manipulation (e.g. wavelength selection and/or intensity modulation) [8]. Moreover, novel manufacture of lenses (e.g. microlens and metalens) and optical filter elements and their integration into imaging systems (e.g. microoptics) though very promising, still relies on complex, time-consuming processes [9,10].

Recent attempts to develop a hand-held optical/fluorescence microscope by coupling a miniaturized version of both lens and filter into a smartphone have mainly relied on scaling down the lens/filter components using standard fabrication techniques, coupled with exploiting the computational and networking capabilities resident in the current generation of smartphones [11–14]. These approaches have been very effective, and many useful biological or medical applications have been demonstrated [11–14]. However, the macroscopic manufacturing approach places limitations on both size (i.e. about 50–100 cm^3) and weight (i.e. 100–200 g) of add-on optical modules; these optical devices can be larger than the smartphone itself, and widespread deployment is hindered by the significant costs associated with fabrication of the miniaturized high-quality optical components [11–14].

To address these challenges, researchers have developed strategies to form lenses from readily cast liquid [15] and polymeric (e.g. polydimethylsiloxane - PDMS) [16–18] precursors that generate optical materials of high clarity and high refractive index, and they have employed surface energy minimization techniques to provide the curvature necessary to yield focal lengths in the range of a few mm to boost optical magnification [16–18] and to further improve resolution [16–18]. For instance, moldless fabrication of PDMS lenses with a focal length as small as 2 mm was demonstrated by curing a PDMS droplet hanging from a curved plastic substrate [16]. In-situ curing of liquid PDMS droplets deposited with an inkjet printing process on a preheated smooth surface was used to fabricate lenses with a focal length of 5.6 mm on a glass substrate [16]. Using a moving needle extruder assisted by thermal moldless curing, PDMS lenses with a focal length of 4.5 mm were formed on a glass slab [17]. Finally, planoconvex PDMS lenses with a focal length of 3.4 mm were fabricated by drop-casting of liquid PDMS onto a smooth circular disk of poly (methyl methacrylate), taking advantage of the resistance to spreading of the liquid precursor by incorporation of a sharp edge [18]. To date, none of these microfabrication methods have been shown to allow incorporation of complex optical filters directly into the fabrication process.

Here we report on the moldless preparation of lenses (focal length down to 4.7 mm) with an embedded optical component (e.g. optical filter, resonant cavity, distribute Bragg reflector), thus integrating the concept of both light-shaping and image magnification into a single lens. The fabrication process has well defined parameters that can be adjusted to control lens curvature and optical filtering parameters, with excellent reliability (yield 95%) and low cost

[19]. The lens is self-assembled by drop-casting the PDMS precursor onto the surface of a nanostructured porous silicon or porous silicon oxide film; the mesopores in the nanostructure naturally direct the lens into a nearly hemispherical shape, and lens curvature is controlled by the porosity of the film. The nanostructured porous silicon film is engineered as an optical component during its preparation, and the cured PDMS lens adheres to the nanostructure such that the PDMS lens contains the optical filter in a single monolithic structure. This approach allows independent adjustment of the optical features of both the lens (e.g. numerical aperture, focal length) and the optical filter (e.g. transmittance spectrum). The filter-lens monoliths are self-adherent to the optical window of the smartphone camera, and as a test case we demonstrate acquisition of fluorescence images of tumor cells using a single filter-lens of diameter of 0.5 cm and weight of 10 mg attached to a commercial smartphone. The lens provides magnification sufficient to image single cells, and the integral nanostructured optical filter effectively rejects the blue excitation source while transmitting the red/green fluorescence emitted from the live/dead cellular staining reagents. Further, the lens allows the effective color tuning of a commercial white LED from red to blue and the narrow wavelength selection of the emission of fluorescence dyes, which are of interest in lighting and agriculture, forensic, and biomedical applications, respectively.

Results and Discussion

Moldless preparation of silicone lens on porous silicon

Figure 1(a) shows a sketch of the main steps involved in the preparation of PDMS lenses on PSi. Prior to formation of the PSi samples, the wafer was cleaned using a sacrificial etching procedure as previously described [20]. A PSi templating layer was prepared by application of a constant anodic current to a clean, highly doped p-type silicon wafer in an aqueous HF-ethanol electrolyte (details are given in the Materials and Method section). A calibrated mass of uncured PDMS was then dropped onto the PSi surface using a small nozzle. Once it contacted the PSi surface, the PDMS droplet formed an oblate spheroid cap due to the balance of adhesive and cohesive forces involved in surface wetting and gravity [21–23] (Figure 1a). After curing, the as-formed PDMS lens was easily peeled off the host PSi layer, thus achieving a free-standing, nearly hemispherical PDMS lens retaining both mechanical and optical characteristics of PDMS. Figure 1b shows a typical PDMS lens formed on as-prepared PSi, before and after peeling it from the PSi substrate. Real-time movie of the formation of PDMS lens on nanostructured PSi layer is provided as Supporting Information (Movie S1).

A thorough investigation of the dependence of geometrical and, in turn, optical characteristics of PDMS lenses formed on nanostructured PSi was carried out by preparing PSi templating layers with different porosity and thickness values. Porosity and thickness of porous silicon samples is readily controlled by the applied current density and duration of the etch, respectively; etching current densities of 3, 30, and 300 mA cm^{-2} and etching times of 6 s to 30 min were tested. The mass of PDMS used in the droplet was also systematically varied.

The above-mentioned current density and etching time values generated PSi layers with porosity values of 58.5±1.3%, 60.7±1% and 76.5±1.3%, and thickness values of 0.10±0.02

to 30±1 μm, determined from optical reflectance measurements of the PSi layers [24] (Figure S1). The pore morphology (by SEM and AFM measurements, Figure S2, S3) featured randomly arranged cylindrical mesopores with relatively consistent average diameter (about 30 nm) and root mean square (RMS) roughness (about 5 nm), regardless of the etching current density value. This is consistent with the sacrificial etching procedure used to clean the wafers prior to PSi formation, as it generates a nanostructured texture on the silicon surface that serves to nucleate pore growth. The surface nanotexture is mainly responsible for determining the average pore diameter of the PSi layer, whereas the current density value used to etch the PSi layer is mainly responsible for the porosity of the PSi layer [20].

Figure 1c (and Figure S4–S6) summarizes both geometrical (i.e., diameter, height, contact angle) and optical (i.e. focal length, numerical aperture) characteristics of PDMS lenses formed using a constant PDMS mass of 10 mg on as-prepared PSi layers with different porosities and constant thickness (10 μm). The optical characteristics of the lens elements were calculated under the approximation of paraxial optics [25], that is, with the lens operating on a narrow region around the lens axis relative to the lens diameter, using the ellipse apex curvature obtained from the lens profile fitting (Figure S4a–d). In fact, Bond number B_0, that is a measure of the gravity/surface force balance, is between 0.38 and 1 (calculation details in the Supporting Information) for PDMS mass ranging from 3.5 to 16 mg (0.75 for 10 mg PDMS drops), respectively, so that though surface forces still dominate, gravity affects the lens profile that is deformed from a circle to an ellipse [22]. Plano-convex lenses suffer from spherical aberrations that impact imaging fidelity (Figure S4e). The third order aberration theory provides a valid analytical tool to take spherical aberrations of plano-convex lenses into account [26]. The porosity value of the PSi layer strongly affected both geometrical and optical features of the PDMS lenses. Moreover, exposure of the samples to vacuum during casting/curing of PDMS and the temperature at which curing of PDMS was carried out also played a significant role, especially for PSi samples of lower porosity (Figures S5 and S6). The mean diameter of the lenses formed on the PSi layers showed an inverse relationship to the porosity of the PSi template used: lens diameters ranged from 4 mm (contact angle 70°, height 1.1 mm) to 3 mm (contact angle 105°, height 1.5 mm) for PSi porosity values of 60% and 77%, respectively. We propose that these diameters were determined by the underlying nanostructure and the degree of infiltration of the liquid PDMS resin into the nanopores of the PSi substrate, in accordance with the Wenzel/Cassie-Baxter hybrid model of liquid wetting of rough surfaces. In this model, the curvature of a droplet in contact with a surface is influenced by both roughness of the surface (via a parameter known as roughness ratio, defined as the ratio of the actual area of the solid surface to its apparent area) and degree of infiltration of the liquid inside the pores [23]. The amount of resin infiltrated into the PSi layers was independently quantified from the optical reflectance spectrum of the PSi layers. These layers display Fabry-Pérot interference, and the interference spectrum is related to the fill fraction of the porous layer, as has been established previously [27] (Figure S6c–d). Accordingly, the focal length (f) of the lenses decreased from 6.5 to 4.7 mm as the porosity of the templating PSi layer increased from 60% to 77%, leading to an increase of the numerical aperture (NA) from 0.28 to 0.31. Control experiments performed on both flat and oxidized silicon substrates showed no lens formation with PDMS; rather, the same volume of PDMS dropped onto a flat silicon wafer spread over the substrate to form a relatively flat film.

We next evaluated the geometrical and optical characteristics of the PDMS lenses formed when the porosity of the PSi layer was held constant, but the thickness of the PSi layer was varied. Figure 1d shows the characteristics of lenses formed by dropping 10 mg of PDMS on PSi layers with thickness values ranging from 0.1 to 30 μm, where the porosity was maintained at a value of 60% (Figure S7). The lens diameter was 4.6 mm on PSi layers with thickness of 100 nm, and it steadily decreased with increasing PSi layer thickness, until a value of 3.6 mm was obtained for a layer thickness of 10 μm. The lens diameter did not change upon further increasing of the PSi layer thickness (up to 30 μm). The free volume in a PSi layer that is 60% porous, 10 μm thick, and 3.6 mm in diameter is 60 nL, which represents ~0.6% of the total volume of the PDMS droplet. Consistently, numerical aperture (NA) increased with PSi thickness: for the 60% porosity PSi film, the NA attained a value of 0.31 (minimum was 0.2 for 100 nm-thick PSi film). The corresponding focal length decreased from 10.5 mm for the 100 nm-thick PSi film to a value of 6 mm for films PSi thicker than 10 μm. These findings are consistent with the Wenzel/Cassie-Baxter hybrid model to the extent that the increasing thickness of the PSi film in the range of 100 nm to 10 μm generated an increase in entrapped air inside the structure, thus increasing the contact angle. As the PSi film further increased in thickness, the polymer reached a limit where it no longer completely infiltrated the porous layer, transitioning a Cassie-Baxter dominating model [23]. The high viscosity and surface energy of the liquid PDMS allowed no further infiltration into the ~30 nm pores, and the curvature of the droplet was no longer controlled by PSi film thickness.

Next we investigated the effect of volume of the uncured liquid PDMS precursor on the quality of the resulting PDMS lens for fixed values of PSi substrate porosity and thickness. Figures 1e–1g gives the geometrical and optical characteristics of the PDMS lenses obtained using a mass of liquid precursor ranging from 3.5 to 16 mg, deposited onto PSi layers of thickness 10 μm and porosity 60% (Figure S8). Remarkably, both diameter (height) and focal length increased with PDMS volume, from 2.7 (0.95) to 5 (1.3) mm and from 4 to 9 mm, respectively. The numerical aperture decreased in this range from 0.31 to 0.25. Therefore, changing the PDMS volume provided an additional parameter to control the characteristics of the resulting PDMS lens.

The contact angle for a liquid often depends on the chemical nature of the solid surface, as this plays a role in the free energy of the liquid-solid interaction. is consistent with the hybrid Wenzel/Cassie-Baxter model, in which entrapped air in the PSi nanostructure after PDMS infiltration plays a significant role. The lenses discussed above all used freshly prepared porous Si films, which display a relatively hydrophobic Si-H surface. We thermally oxidized some PSi substrates (750 °C in air for 120 min) in order to generate relatively hydrophilic silicon oxide surfaces. The geometry and optical properties of the resulting PDMS lenses differ up to 20% from lenses prepared from the as-etched, Si-H terminated PSi substrates (Figure S9). Such a change in the optical properties (i.e. focal length and NA) has to be considered when designing PDMS lenses on top of oxidized PSi. Changing the crosslinking ratio of the PDMS, by changing the ratio of base to curing agent from 10:1 to 20:1, did not dramatically change the properties of the resulting lenses (Figure S10).

We next characterized the lenses in set of a high-resolution imaging tests. For these experiments, free-standing PDMS lenses with focal length of 4.7 mm were prepared, using a PSi layer with thickness of 10 μm and porosity of 76.5%, and 10 mg of PDMS. The lens was directly attached to the built-in camera of a commercial smartphone (Samsung Galaxy S5, see Supporting Information for details). A detailed analysis on how direct coupling of a lens to a smartphone camera affects the imaging performance can be found in [28,29]. The excellent adhesive property of PDMS on glass surfaces allowed the PDMS lens to be firmly, though reversibly (> 100 times), attached to the glass window of the camera without the use of adhesives or supporting fixtures. A chromium-on-quartz optical resolution test pattern (5 mm × 5 mm) featuring an array of parallel lines with constant duty-cycle δ=0.5 (δ defined as the ratio between line width and line spacing) and width (spacing) sequentially reduced from 250 to 4 μm was used to investigate quality and resolution of images acquired with the smartphone equipped with the PDMS lens. Control images were acquired using the as-received smartphone, that is without any external lens attached to the camera. Figure 1h shows typical images acquired using the smartphone equipped with the PDMS lens; an image acquired with the bare smartphone (i.e. without PDMS lens) at the maximum allowable digital magnification (3x) is given in the inset for comparison.

The PDMS lens clearly resolved all the lines of the test pattern, from a maximum width of 250 μm to a minimum width of 15 μm. Application of 3x digital magnification to the smartphone camera resolved features as small as 4 μm (Figure 1i). The greyscale intensity profiles extracted for the various lines in Figure 1h, 1i yielded a signal-to-noise ratio (SNR) greater than 10 for all lines with width ranging from 250 to 15 μm (inset in Figure 1i and Figure S11). Not all the 4-μm-wide lines imaged over a length of 250 μm were consistently resolved; this can be attributed to non-uniform illumination of the pattern and lens aberrations. On the other hand, all the lines with width of 8 μm were well resolved (S/N=15). The empirically determined 125 lp mm^{-1} (that is, 1 line-pair in 8 μm) resolution reported for the PDMS lens here is reasonable, considering the spherical aberrations expected from a plano-convex lens and the limitations of the camera image sensor of a smartphone (see Supporting Information) [28,29].

Monolithic silicone lenses embedding porous silicon optical components

With an optimized process to generate PDMS lenses in hand, we next developed a means to incorporate optical filtering components (e.g. Bragg reflectors, rugate filters, resonant cavities) into the lenses. This aspect of the work was enabled by the electrochemical fabrication process used to prepare the PSi substrates, which is readily adapted to generate one-dimensional porous optical filters [30–35] for a variety of applications [36–41].

The preparation is schematically depicted in Figure 2a. After cleaning of the Si substrate, we prepared a PSi templating layer with porosity of ~77% and thickness of ~1 μm (etch current density = 300 mA cm^{-2}; etch duration = 7 s) (Figure 2a-1) so as to guarantee the formation of a PDMS lens with high contact angle and, in turn, short focal length (Figure 1c,d). The formation of a porous layer is always initiated at the interface between the porous Si layer and the crystalline Si substrate; thus once this layer was formed, a subsequent electrochemical etch could be used to generate the optical filter element, and this element was physically located beneath the initial PSi template layer. This approach enabled separate control over the morphology of the PDMS lens and the optical component to be integrated in the lens. Once the PSi templating layer was prepared, we next etched a thin (200 nm) barrier layer of PSi with lower porosity (58%) (etch current density = 3 mA cm^{-2}; etch duration = 50 s) to inhibit flow of the liquid PDMS pre-polymer into the optical component (Figure 2a-2). The reason that the PDMS needed to be excluded from the optical filter was that the refractive index of PDMS is similar to the refractive index of oxidized PSi; if it infiltrated the PSi optical component, index matching would result in a significant loss of spectral filtering ability of the PSi optical component.

We evaluated three types of spectral filtering elements in this work: a distributed Bragg reflector (DBR), a rugate filter, and a resonant cavity. The optical element of interest was sequentially etched underneath the PSi barrier layer using the appropriate current-time waveform: a square wave for the DBR, a sine wave for the rugate filter, and two DBRs separated by a 1/2 wave layer for the resonant cavity (Figure 2a-3) [24,42]. After the PSi optical component was etched, the current density was increased to 700 mA cm^{-2} for 0.5 s to produce a high porosity (porosity >90%) layer at the bottom of the PSi stack. The purpose of this last layer was to act as a readily sheared release layer, to facilitate detachment of the PDMS lens and the PSi optical component as a single monolith from the silicon wafer. The total thickness of the PSi stack was set between 10 to 15 μm.

Prior to lens formation, the as-prepared PSi stack was thermally oxidized (750°C in air, for 120 min) to fully convert the elemental silicon in the component into silicon oxide (Figure 2a-5). This oxidation step had a twofold aim: first, it eliminated optical absorbance of the silicon crystallites in the PSi stack by converting elemental Si to SiO_2. Separate experiments established that the broad absorbance of silicon throughout the visible spectrum exerted a negative effect on light transmission through the PSi stack that substantially reduced the fidelity of the spectral filter. Second, oxidation of the PSi structure reduced the overall refractive index contrast between the barrier and the templating layers of the PSi structure; these layers acted as Fabry-Pérot interferometers for white light that strongly affected the reflectance/transmittance spectrum of the PSi component. Reduction of index contrast by conversion of the high index Si component to a relatively lower index SiO_2 component substantially reduced the Fabry-Pérot features in the transmission spectrum of the final filter-lens hybrids.

The filter-lens hybrids were then prepared by contacting a 10 mg mass of the PDMS precursor to the surface of the oxidized PSi stack. The PDMS precursor infiltrated both the templating and the barrier layers, self-assembling into a hemispherical PDMS lens (Figure 2a-6). After thermal curing at 120 °C for 1h, the PDMS lens embedded with the PSi optical component was peeled from the silicon wafer support by dropping a small volume (20 μL) of a dilute aqueous hydrofluoric acid solution to dissolve the small quantity of silicon oxide in the release layer surrounding and beneath the lens assembly (Figure 2a-7,8). The rest of the PSi stack did not noticeably dissolve under these conditions, despite the fact that the stack had been thermally oxidized to SiO_2. Presumably, lower molecular weight PDMS oligomers had diffused throughout the structure sufficiently to mask the PSi structure, making it less susceptible to attack by aqueous HF.

Figure 2b, c (and Figure S12) show cross-sectional and plan-view SEM images of a PSi stack featuring a DBR filter etched underneath PSi templating and barrier layers. The as-prepared DBR was designed with a photonic bandgap centered at 500 nm and consisted of 80 bilayers with porosity alternating between 65% and 80%, corresponding to a dielectric stack with n = 1.57 and 1.29 (calculated using the Bruggemann equation) and thickness of ~62 nm and ~91 nm, respectively (Figure S13). Figure 2b shows a cross-sectional electron microscope image of the as-prepared PSi stack, with total thickness of ~13.5 μm, and Figure 2c provides a close-up view of the templating layer, the barrier layer, and a portion of the DBR structure, with darker/brighter regions visible along the direction perpendicular to the wafer surface corresponding to higher/lower porosity regions. The detailed morphology of the barrier layer is shown in the inset of Figure 2c. The higher porosity templating layer features columnar-like pores with diameter of about 20 nm running from top to bottom; by contrast, the barrier layer (low porosity) features pine tree-like pores with diameter of a few nm. The DBR structure has columnar-like pores with highly regular low and high porosity layers with thickness of 62 and 91 nm, respectively, as obtained from the optical porosity analysis of Figure S13, which are in good agreement with the design parameters.

Reflectance (and transmittance, when feasible) spectra collected at each preparation step of the lens are reported in Figure 2e–g for a PDMS lens incorporating a PSi DBR filter of the type reported in Figure 2b, c. A photograph of the integral PDMS lens-PSi filter assembly after detachment from the silicon chip is shown in Figure 2g (inset).

The reflectance spectrum of the as-prepared PSi stack (i.e. before oxidation) showed a main peak around 500 nm, where the photonic bandgap of the DBR was centered by design, with multiple shoulders due to the presence of both templating and barrier layers etched on top of the DBR structure (Figure 2b, c). These two layers act as back-scattering interferometers, so that the resulting reflectance spectrum arises from the interference of the DBR spectrum with the Fabry-Pérot interference spectrum coming from both the templating and the barrier layer. On the other hand, the extended pattern of interference fringes at wavelengths longer than 550 nm results from constructive/destructive interference of light within the entire PSi stack. After thermal oxidation of the PSi stack, the reflectance spectrum was mainly determined by the DBR structure, with a well-defined, high reflectance region corresponding to the photonic bandgap of the structure, centered now around 400 nm, and low reflectance regions outside the photonic bandgap (Figure 2f). The decrease in the spectral interference shoulders observed upon oxidation of the samples is attributed to the lower refractive index contrast of both the templating and the barrier layers, which become transparent to visible radiation after full conversion of crystalline silicon into silicon oxide. The position of the stop-band of the DBR blue-shifted by approximately 100 nm, from 500 to 400 nm, upon oxidation due to the lowered refractive indices of both high and low porosity PSi layers.

Figure 2g shows both reflectance and transmittance spectra of the free-standing PDMS lens embedded with the DBR filter, i.e. after the PDMS lens-PSi filter assembly was removed from the silicon chip (inset in Figure 2g). The lens featured geometrical and optical characteristics that were in good agreement with those achieved for the bare PDMS lens (i.e. without any PSi optical filter component) prepared on a similar templating PSi layer (porosity 76%, thickness of 10 μm) oxidized at 750°C (Figure S9). Remarkably, both reflectance and transmittance spectra of the DBR structure were relatively well retained after the lens assembly was removed from the silicon chip. This corroborates the hypothesis above-made that diffusion of oligomers throughout the whole PSi stack underneath the barrier layer protects the oxidized PSi skeleton from HF etching during the lens detachment process. The photonic stop-band was clearly defined, with a transmittance intensity approaching zero and the corresponding reflectance intensity >90% in the photonic bandgap region of the spectrum; moreover, the lens displayed high transmittance (>90%) and low reflectance (<10%) outside the photonic stop-band, with minimum optical scattering losses. The high quality of the filter was apparent in the high rejection ratio observed (the ratio between pass-band and stop-band intensity for transmitted light was >100). The quality factor (Q) of the DBR was ~ 9, with a stop-band width of ~ 50 nm and center wavelength of ~ 450 nm. These values were 2x larger and 35 nm red-shifted, respectively, relative to the oxidized DBR before lens formation. This is attributed to partial infiltration of PDMS in the DBR structure, which can be expected to increase the effective refractive index of the structure. Although the optical measurements indicated that both the PSi templating and barrier layers were completely filled with PDMS by the process, and the majority of the PDMS did not flow past the barrier layer, it is likely that smaller molecular weight oligomers of lower viscosity were able to penetrate the barrier layer and coat the surface of the DBR structure. As mentioned above, these lower molecular weight components are likely responsible for the resistance of the DBR layer to attack by HF. The relatively small shift in the stop band upon PDMS lens formation indicates that silicone only partially infiltrated the DBR. The refractive index of silicone and silica are indeed sufficiently similar (1.43 and 1.46, respectively), that full infiltration of the nanopores of the DBR structure by silicone would have led to a significant degradation of the spectral features of the DBR. Figure S14 shows the reflectance and transmittance spectra of an oxidized PSi optical component that was prepared without and with a barrier layer on top, before and after PDMS lens formation. The optical features of the designed PSi component were retained after lens formation (and detachment from the optical substrate) in the presence of the barrier layer; conversely, the spectral signatures of the PSi optical component vanished in the absence of the barrier layer due to the considerable infiltration of PDMS in the PSi stack, which eliminated the refractive index contrast in the porous nanostructure.

The experimental spectra were best-fit to theoretical spectra calculated using the transfer matrix method in order to refine and validate the porosity/refractive index and thickness relationships of the various PSi layers (Figure S15), and to estimate the extent of PDMS infiltration in the different PSi layers as discussed above (Figure S16). Spectra at each step in the preparation generally showed excellent agreement between experiment and theory. The calculations confirmed that PDMS fully infiltrated both templating and barrier PSi layers, and that only 50% (on average) of the DBR structure was infiltrated by silicone.

The optical filtering capability of the PDMS lens-PSi filter could be tuned over the UV-vis-NIR range by setting the position of the photonic stop-band of the DBR embedded in the lens. In the porous Si system this can be readily achieved by appropriate selection of the period, amplitude, and duty cycle of the square wave in the current density waveform used to prepare the sample. Figure 3a shows the transmittance spectra of three PDMS lenses that contained embedded DBR structures, where the stop-band center was systematically adjusted to appear in different regions of the visible spectrum, from blue to red. The periods of the square waves used to prepare the DBR structures were 4, 4.5, and 5 s for the blue, green, and red filters, respectively. All waveforms used a constant duty-cycle (i.e. ratio between duration of the etching time for the high porosity layer and the overall period of the waveform). As the period of the waveform was increased, thicker high and low porosity layers were prepared, which led, in turn, to a red-shift of the photonic stop-band. These DBR structures were designed to act as stop-band filters centered in different regions of the visible spectrum, so that they could selectively remove specific wavelength ranges (i.e. colors) from the spectrum of light transmitted through the PDMS lens-PSi filter assembly.

The yield of the fabrication process for PDMS lens embedding PSi optical components, defined as the ratio between the number of PDMS/PSi lenses that featured experimental (measured) optical properties consistent (maximum change of 20%) with the design (i.e., focal length and NA for the lens and transmittance spectrum for the optical component) and the total number (>100) of manufactured lenses, was ~ 95%.

We next explored a range of possible optical filter types for the PDMS lens-PSi filter assemblies. The use of the templating and the barrier PSi layers in the design essentially decoupled the geometric parameters of the PDMS lens (in terms of curvature, numeric aperture, etc.) from the spectral filtering features of the PSi component. This enabled the incorporation of a wide range of optical filter elements into the design without compromising magnification. For instance, when a sine-wave current density waveform was used to etch the PSi optical component, the resulting PDMS lenses incorporated a rugate filter that displayed a narrow notch in optical transmittance (quality factor Q=26). Figure S17 shows both transmittance spectra and images acquired with several PDMS lenses that incorporated such notch filters centered at different wavelengths, from blue to red. The central wavelength of the rugate filter was tuned by changing the period of the sine wave in the current density waveform.

A microcavity type of optical filter was also designed into the PDMS lens-PSi filter element. For this structure, two identical DBR waveforms (square-wave current density) with constant duty-cycle were separated with a single cycle (in the middle of the profile) in which the duty-cycle value was twice the value of the DBRs, generating a half-wave plate in between the two DBR mirrors (ten bilayers each). Several of these resonant cavity types of filters, operating at different wavelengths in the visible range and with an average Q-factor of 140, were prepared. The DBR waveform period determined the color of the microcavity as follows: 3.5 s (blue lens), 4 s (aquamarine lens), 4.25 s (green lens), 4.5 s (orange lens) and 5 s (red lens) (Figure S18). The duty-cycle was maintained at a constant value for all of these samples. Figure 3b shows transmission spectra of three PDMS lens-PSi filter elements prepared with their resonant cavity centered at blue, green, and red wavelengths.

Application of monolithic silicon lens embedding porous silicon optical elements to fluorescence imaging and light shaping

We next explored the potential utility of the PDMS lens-PSi filter assemblies as compact, low-cost, high-resolution imaging elements for a commercial smartphone, which could be of interest for various in-field applications in low-resource settings.

As a first case study, simultaneous image magnification and separation of light into a single-color component was investigated using three PDMS-PSi lenses with focal length 5.75 mm that incorporated blue, green, and red PSi optical filter components (Figure 3a). A bare PDMS lens, i.e. without the PSi optical filter, with similar focal length was used as a control lens. Photos of both filtering and bare lenses placed on a black background are shown in Figure 3c. The blue-filtering lens appears blue in these images, because that is the color of the rejection band reflected from the DBR embedded within the lens; in a similar way, green and red-filtering lenses appear green and red, respectively. The lenses were mounted onto a smartphone camera (Samsung S5) and used to image a 4 mm × 4 mm grayscale picture of Marie Curie (Figure 3d). The magnified image acquired with the control PDMS lens appeared gray, consistent with the fact that no PSi optical component was embedded in the lens (Figure 3d, top-left). Images acquired with the PDMS-PSi lenses were able to separate the image into the CMY color components (Figure 3d). Thus, the image appeared magenta with the green-filtering lens, cyan with the red-filtering lens, and yellow with the blue-filtering lens, which are the complementary colors of those filtered by the lenses [43].

Similar experiments were carried out with different PDMS lenses featuring blue, green, orange, and red-filtering PSi rugate-filters (Figure S17). Due to the higher Q factor (about 26) of the PSi rugate filters, only a small portion of a given color band was filtered out, so that the effect of light filtering on the acquired images was not as marked as that achieved with PSi DBR components (Q=9). Thus the rugate filter elements are more suitable as notch filters for specific wavelengths. The notch filter is a common optical element used in Raman spectroscopy and Raman imaging.

We next investigated a fluorescence microscope imaging application that utilized a smartphone as the imaging system. For fluorescence microscopy, the optical path must simultaneously filter out a specific excitation wavelength (e.g. either blue or green excitation) and enable the collection of an emitted wavelength (e.g. either green or red emission). We first characterized the optical transmission spectrum of the PDMS lens-filter combinations in order to develop a lens optimized for the dyes and excitation sources we planned to use. Experiments were carried out with PDMS lenses placed in the optical path of a probe fed into an Ocean Optics CCD spectrometer/fluorimeter. Figure 3e shows a typical white light transmittance spectrum of a PDMS-PSi lens containing an embedded DBR filter (black trace). The spectrum shows strong rejection of wavelengths in the range 450 to 480 nm. We then replaced the PDMS-PSi lens with a bare PDMS lens (one containing no embedded PSi filter) and acquired the emission spectrum of a thin film of the polymer F8BT, which fluoresces in the green (550 nm) when excited with a blue (456 nm) LED. When no PSi filter was used, the spectrum displayed the emission band of the polymer along with the spectral emission of the LED excitation source (Figure 3e, blue trace). We then acquired the same spectrum but with the PDMS-PSi filter lens in the optical path. This spectrum (Figure 3e, red trace), showed excellent rejection of the blue LED light while retaining the strong green emission spectrum from the F8BT target.

After verifying the ability of the PDMS-PSi lens-filter assembly to reject the blue excitation source and pass the green emission of the polymer test target, we then affixed a blue-filtering PDMS-PSi lens to the front of the camera of a commercial smartphone (Samsung S5) and collected fluorescence images (Figure 3f). We used green fluorescent polymer beads (λ_{em} = 515 nm) of diameter 53–63 μm, in order to emulate the dimensions of mammalian cells. Figure 3 compares images acquired using the smartphone equipped with a bare PDMS lens (Figure 3g) and a PDMS lens embedded with a blue-filtering PSi DBR (Figure 3h). In both cases, the microbeads were resolved by the lenses. The blue excitation light was not filtered by the bare PDMS lens, and in this image the beads appear blue because the green photoluminescence was almost completely obscured (Figure 3g, S19). By contrast, the PDMS lens that contained the embedded PSi DBR blue filter effectively removed the blue excitation light, and the green fluorescence from the microbeads was apparent (Figure 3h, S19). Thus, the PDMS-PSi lens was able to effectively transform the smartphone camera into a hand-held fluorescence microscope.

The capability of the fluorescence imaging system was next validated in a proof-of-concept experiment involving the imaging of CAVO-3 ovarian cancer cells using a conventional live/dead assay. The fluorescent dyes calcein AM (live stain, $\lambda_{ex}/\lambda_{em}$ = 494/517 nm) and ethidium homodimer-1 (dead stain, $\lambda_{ex}/\lambda_{em}$ = 528/617 nm) were used, and a smartphone equipped with a PDMS lens embedded with a PSi DBR filter was used to capture the images.

For the dead cell assay, the CAVO-3 cells were treated with 10% DMSO prior to staining and fixation. The optical setup mimicked an inverted microscope configuration (Figure 4a). Briefly, the PDMS-PSi lens (with focal length 5.75 mm) was fixed to the camera on an Axon 7 (ZTE) smartphone (20 MP) and the laser excitation beam was positioned at a 60–70° angle normal to the optical table. The PSi DBR filter was designed to exclude light from the camera for wavelengths between 465–525 nm (Figure 4b). A bare PDMS lens (no PSi filter) with comparable focal length was used for control experiments. The slides containing the cells were mounted on a three-axis adjustable stage. The smartphone was controlled remotely by computer using a commercial application (IP webcam) and the live-dead cells were imaged sequentially using 495 nm and 517 nm excitation (Figure 4c, 4d and Figure S20).

As expected, the bare PDMS lens allowed cells on the slide to be imaged, though it did not filter out the excitation light at either wavelength. The cells strongly scattered the excitation light and appeared as bright hotspots in the images. The scattering from the glass slide and cells was much stronger in intensity than the fluorescence, so that red or green fluorescence could not be consistently observed. With the bare lens the two-color channels are separated by the built-in filters of the color camera in the smartphone, which are not as spectrally pure as the bandpass filters used in a confocal microscope, so that light from the excitation source provides a significant interference that overwhelms the information contained in the red or green color channels (Figure 4d, “bare PDMS lens” images). The PDMS/PSi lens overcomes this limitation by removing the (495 or 517 nm) excitation sources, as the PDMS/PSi lens is a single channel filter designed to reject both the 495 nm and 517 nm excitation sources, allowing the fluorescence from the cellular stains to be readily visualized (Figure 4d, “PDMS/PSi lens” images). The live and dead cells can now be clearly identified from the respective green and red fluorescence images (Figure 4c and Figure 4d, “PDMS/PSi lens” images). Although the smartphone camera is a full color imager, we did not select specific digital color channels for the images shown in this paper, in order to more fully illustrate the effects of the optical filters.

The excitation spectrum of the ethidium homodimer-1 was broad, and it overlapped with the excitation spectrum of calcein somewhat (Figure 4b). Therefore, the shorter wavelength (495 nm) excitation source used in these experiments excited both dyes to some extent and it could be used for both assays, without 517 nm excitation (Figure 4d, “PDMS/PSi lens λ_{ex}=495 nm” images). For purposes of this paper and to be consistent with standard assays, the images of Figure 4 were acquired using the two separate excitation sources (495 and 517 nm). The stop-band of the PSi DBR used for those images was configured to block both 495 nm and 517 nm excitation sources. This allowed the use of a single PDMS-PSi lens to image fluorescence signals from both live and dead cells, without needing to switch lens/filter sets. The image quality allowed standard cell counting using ImageJ software [44] (Figure S21).

As a control, the live cells were imaged using 450 nm excitation, which can excite the dye but is just outside the filter cut-off (~465 nm). Therefore, this blue excitation light bled through to the camera, degrading image fidelity substantially (Figure S20c, d). Confocal images were collected using a laboratory-grade microscope, operating at comparable magnification, in order to confirm live/dead status of the cells and to benchmark the quality of images obtained with the PDMS-PSi lens-smartphone configuration (Figure 4d, “Fluorescence microscope” images, and Figure S22). Relative percentages of live/dead cell counts were comparable for the two imaging systems. Despite the obvious superiority of the confocal microscope in terms of resolution, image contrast, and fidelity, the PDMS-PSi lens-smartphone system performed surprisingly well considering its cost, portability, and ease of use.

The ability of the monolithic PDMS/PSi lens elements to filter light with high spectral fidelity led us to explore their applicability for lighting applications [45]. We found that the color of a commercial warm-white LED could be adjusted from red to blue by engineering the appropriate DBR or resonant cavity into the porous silicon filter portion of the PDMS/PSi lens element (Figure 5a). For this configuration, the PDMS/PSi lens was placed on top of a commercial white LED and the spectrum of light transmitted through the lens was acquired. The experimental results are summarized in Figure 5b,c (and in Figure S23 for resonant cavities). The emission spectrum of the bare LED (i.e. without any lens), was used as reference spectrum; the emission spectrum of the LED coupled to a bare PDMS lens (i.e. without any PSi filter embedded) was used as control (Figure S23). Transmission spectra in Figure 5b show that the filter was capable of attenuating the spectrum of the LED emission at specific wavelength intervals (those falling in the stop band of the DBRs), thus providing a simple means to shape the color of light transmitted through the lens. Data from representative samples are shown superimposed on a CIE 1931 diagram in Figure 5c.

Finally, the ability of the elastomeric lens-optical filter composites to select very a narrow wavelength slice from the relatively broad emission spectrum of a fluorescent molecular probe was demonstrated. This is of interest in forensics or agriculture studies [46] or narrowband vasculature imaging [47]. For these experiments, the porous silicon resonant cavities embedded in the PDMS/PSi lens displayed a narrow resonance band whose wavelength was within the fluorescence emission spectrum of fluorescein or rhodamine B. The fluorescence spectrum from the relevant dye was then collected through the composite lens assembly and compared to the spectrum of the dye measured with no PDMS/PSi lens assembly, as a reference (Figure 5d,e). For both dyes, the intrinsic broad (> 100 nm) fluorescence emission spectrum was effectively narrowed to 5 nm (full width at half maximum – FWHM) at the resonant wavelength of the cavity. The high numerical aperture of the lens used in collection mode increased the acceptance angle of the emitted light relative to a detector that employed no lens.

Conclusions

In summary, the robust (yield >95%) and inexpensive method to prepare lens-optical filter combinations using PDMS and porous silicon integrated two basic optical concepts of image magnification and light shaping into a single lightweight lens. We demonstrated the potential of this technology for compact, low-cost, hand-held microscopy using a smartphone, which could make a substantial impact in low-resource settings.

This was achieved by leveraging the spontaneous self-assembly of PDMS into a hemispherical lens, directed by a nanostructured porous silicon layer. The porous silicon nanostructure was engineered as an optical component, which became fixed to the PDMS as it cured. The process was optimized to set the optical parameters (i.e. focal length, NA) of the lens independent of the optical characteristics of the filter; bandpass, notch, and resonant cavity filters were demonstrated. The bandpass structures were utilized to demonstrate two notional applications where high-fidelity spectral filtering is important--in a cellular fluorescence assay and as a color filter for white LED lighting.

The main fundamental advance presented in this work is in the nanostructure design, which allows self-assembly of a lens without a mold, control of both lateral and depth flow of a pre-polymer solution, and a means to very inexpensively integrate a high-fidelity optical component into a single monolithic structure. All of these elements represent fundamental advances in nanoscale control of materials properties that have not previously been demonstrated and dramatically simplify the process of preparing multi-functional optical elastomeric elements at low cost and in a process with a low degree of complexity. Although the approach was demonstrated using PDMS as the optical lens element, we envisage that engineering polymers with different mechanical and optical properties, such as polycarbonate, could also be used. Furthermore, because the anisotropic nanostructure of porous silicon is capable of polarizing light [48], it may be possible to fabricate polarized lens elements using the proposed approach.

Supplementary Material

Refer to Web version on PubMed Central for supplementary material.

Acknowledgments

G.B wants to acknowledge the EU H2020 ETN SYNCHRONICS under grant agreement 643238 for partially supporting this work. G.B. wants to thank Dr. F.F.R. Toia (STMicroelectronics, Milan) for technical assistance with SEM images. J. Wang thanks the NIH for a predoctoral training grant 2T32CA1539106A1 (CRIN). B. Kim thanks the NIH for grant R01 AI132413-01 and the University of California at San Diego's Dissertation Fellowship for support.

References

[1]. "The Nimrud lens / the Layard lens". Collection database. The British Museum https://www.britishmuseum.org/research/collection_online/collection_object_details.aspx?objectId=369215&partId=1. Accessed December 10th, 2018

[2]. Van Helden A, Dupré S, Van Gent R, The Origins of the Telescope, Amsterdam, University Press, Netherlands 2010, p. 24.

[3]. Rose J, Nature 1964, 201, 653.

[4]. Rosenthal CK, Nat. Milestones 2009, 2009.

[5]. Heinrichs A, Nature 2009, 11, S6.

[6]. Zhang L, Liu W, Front. Mech. Eng 2017, 12, 3.

[7]. Yuan W, Li L-H, Lee W-B, Chan C-Y, Chinese J Mech. Eng 2018, 31, 16.

[8]. Reivhman J, Handbook of optical filters for fluorescence microscopy. Chroma Technology Corporation, U.S.A 2010.

[9]. Camposeo A, Persano L, Farsari M, Pisignano D, Adv. Opt. Mater 2019, 7, 1800419. [PubMed: 30775219]

[10]. Khorasaninejad M, Capasso F, Science 2017, 358, eaam8100. [PubMed: 28982796]

[11]. Koydemir HC, Ozcan A, Future Microbiol 2017, 12, 641. [PubMed: 28541094]

[12]. Ballard ZS, Brown C, Ozcan A, ACS Nano 2018, 12, 3065. [PubMed: 29553706]

[13]. Tseng D, Mudanyali O, Oztoprak C, Isikman SO, Sencan I, Yaglidere O, Ozcan A, Lab Chip 2010, 10, 1787. [PubMed: 20445943]

[14]. Wei Q, Qi H, Luo W, Tseng D, Ki SJ, Wan Z, Göröcs Z, Bentolila LA, Wu T-T, Sun R, Ozcan A, ACS Nano 2013, 7, 9147. [PubMed: 24016065]

[15]. Kuiper S, Hendriks BHW, Appl. Phys. Lett 2004, 85, 1128.

[16]. Lee WM, Upadhya A, Reece PJ, Phan TG, Biomed. Opt. Express 2014, 5, 1626. [PubMed: 24877020]

[17]. Amarit R, Kopwitthaya A, Pongsoon P, Jarujareet U, Chaitavon K, Porntheeraphat S, Sumriddetchkajorn S, Koanantakool T, PLoS One 2016, 11, e0146414. [PubMed: 26765524]

[18]. Ekgasit S, Kaewmanee N, Jangtawee P, Thammacharoen C, Donphoongpri M, ACS Appl. Mater. Interfaces 2016, 8, 20474. [PubMed: 27419266]

[19]. Sung Y, Jeang J, Lee C-H, Shih WC, Biomed J. Optics 2015, 20, 047005.

[20]. Mariani S, Pino L, Strambini LM, Tedeschi L, Barillaro G, ACS Sensors 2016, 1, 1471.

[21]. Whyman G, Bormashenko E, Stein T, Chem. Phys. Lett 2008, 450, 355.

[22]. Lubarda VA, Talke KA, Langmuir 2011, 27, 10705. [PubMed: 21812438]

[23]. Yen T-H, Soong C-Y, Phys. Rev. E 2016, 93, 22805.

[24]. Ruminski AM, Barillaro G, Chaffin C, Sailor MJ, Adv. Funct. Mater 2011, 21, 1511.

[25]. Born M, Wolf E, Principles of Optics, Cambridge University Press, Cambridge, UK, 1999.

[26]. Florian C, Piazza S, Diaspro A, Serra P, Duocastella M, ACS Appl. Mater. Interfaces 2016, 8, 17028. [PubMed: 27336194]

[27]. Segal E, Perelman LA, Cunin F, Di Renzo F, Devoisselle J-M, Li YY, Sailor MJ, Adv. Funct. Mater 2007, 17, 1153.

[28]. Jung D, Choi JH, Kim S, Ryu S, Lee W, Lee JS, Joo C, Sci. Rep 2017, 7, 1. [PubMed: 28127051]

[29]. Switz NA, D'Ambrosio MV, Fletcher DA, PLoS One 2014, 9, 5.

[30]. Vincent G, Appl. Phys. Lett 1994, 64, 2367.

[31]. Araki M, Koyama H, Koshida N, J. Appl. Phys 1996, 80, 4841.

[32]. Berger MG, Arens-Fischer R, Thönissen M, Krüger M, Billat S, Lüth H, Hilbrich S, Theiß W, Grosse P, Thin Solid Films 1997, 297, 237.

[33]. Pavesi L, Dubos P, Semicond. Sci. Technol 1997, 12, 570.

[34]. Loni A, Canham LT, Berger MG, Arens-Fischer R, Munder H, Luth H, Arrand HF, Benson TM, Thin Solid Films 1996, 276, 143.

[35]. Thönissen M, Berger MG, Theiss W, Hilbrich S, Krüger M, Lüth H, Solid State Phenom 1997, 54, 65.

[36]. Weiss SM, Ouyang H, Zhang J, Fauchet PM, Opt. Express 2005, 13, 1090. [PubMed: 19494976]

[37]. Piret G, Drobecq H, Coffinier Y, Melnyk O, Boukherroub R, Langmuir 2010, 26, 1354. [PubMed: 20067318]

[38]. Krismastuti FSH, Pace S, Voelcker NH, Adv. Funct. Mater 2014, 24, 3639.

[39]. Gupta B, Mai K, Lowe SB, Wakefield D, Di Girolamo N, Gaus K, Reece PJ, Gooding JJ, Anal. Chem 2015, 87, 9946. [PubMed: 26312479]

[40]. Ocier CR, Krueger NA, Zhou W, V Braun P, ACS Photonics 2017, 4, 909.

[41]. Arshavsky-Graham S, Massad-Ivanir N, Segal E, Weiss S, Anal. Chem 2019, 91, 441. [PubMed: 30408950]

[42]. Robbiano V, Paternò GM, La Mattina AA, Motti SG, Lanzani G, Scotognella F, Barillaro G, ACS Nano 2018, 12, 4536. [PubMed: 29727169]

[43]. Young T, Phil. Trans. R. Soc. Lond 1802, 92, 12.

[44]. Rueden CT, Schindelin J, Hiner MC, DeZonia BE, Walter AE, Arena ET, Eliceiri KW, BMC Bioinformatics 2017, 18, 529. [PubMed: 29187165]

[45]. Ji C, Lee KT, Xu T, Zhou J, Park HJ, Guo LJ, Adv. Opt. Mater 2017, 5, 15.

[46]. McMurtrey JE, Corp LA, Kim MS, Chappelle EW, Daughtry CST, and DiBenedetto JD, in Proc. SPIE 10301, Boston, MA, USA, 2001, 1030104.

[47]. Du Le VN, Wang Q, Gould T, Ramella-Roman JC, Joshua Pfefer T, Appl. Opt 2014, 53, 4061. [PubMed: 24979441]

[48]. Gaponenko SV, Kononenko VK, Petrov EP, Germanenko IN, Stupak AP, Xie YH, Appl. Phys. Lett 1995, 67, 3019.

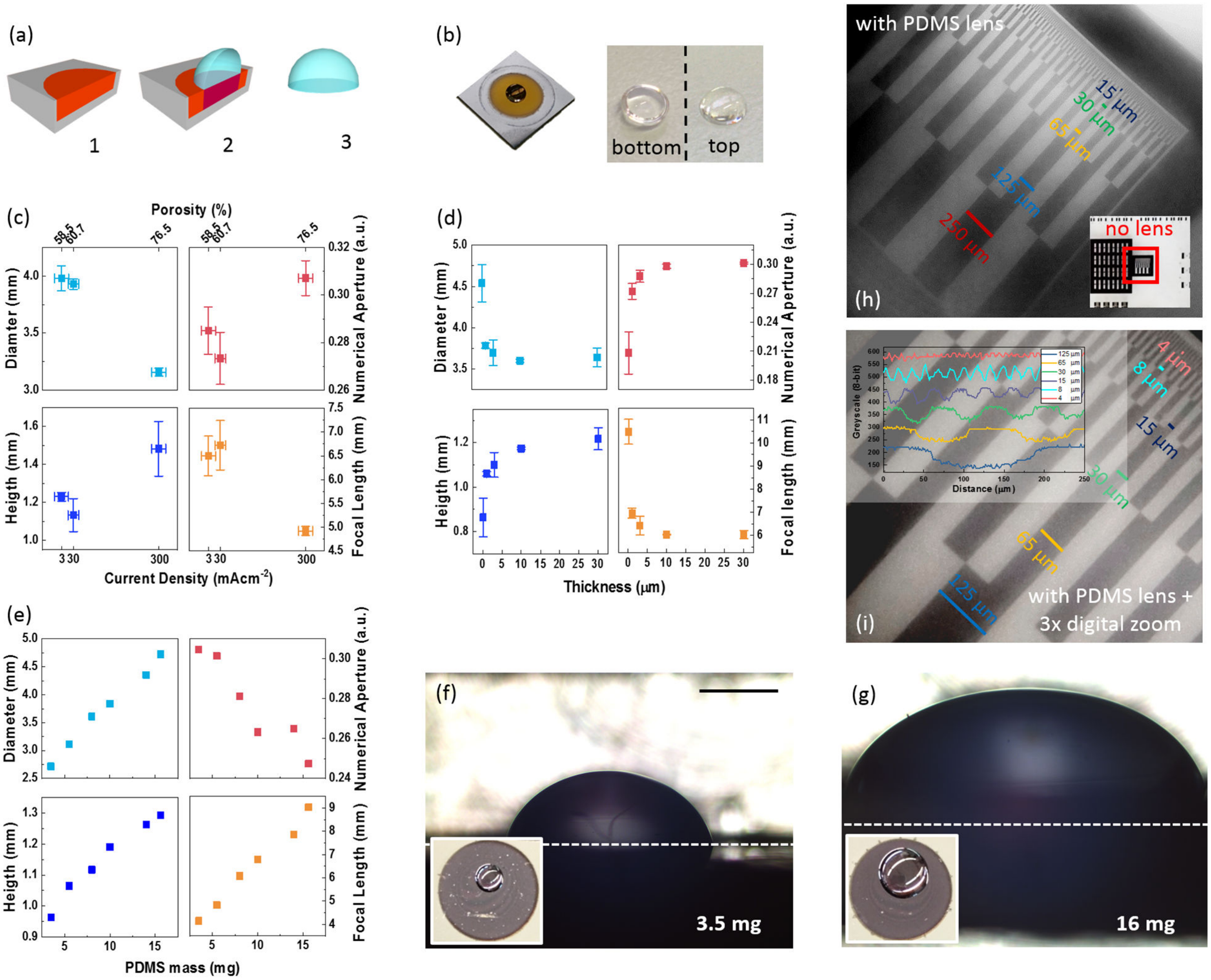

Figure 1. Preparation and characterization of PDMS lenses on nanostructured porous silicon.
(a) Sketch of PDMS lens preparation on nanostructured PSi: 1- etching of a PSi templating layer; 2- drop of a prescribed mass of PDMS pre-polymer on PSi and subsequent thermal curing; and, 3- free-standing PDMS lens obtained by peeling the lens off the PSi chip. (b) Picture of a PDMS lens as-formed on the PSi chip (left) and after peeling it off the PSi chip (right). (c) Main geometrical and optical characteristics of PDMS lenses for different porosity values (and, in turn, etching current density values) of the PSi templating layer, for constant PSi thickness of 10 μm and same PDMS mass of 10 mg. (d) Main geometrical and optical characteristics of PDMS lenses for different thicknesses of the PSi templating layer, at constant porosity of 60.7% and same PDMS mass of 10 mg. (e) Main geometrical and optical characteristics of PDMS lenses for different PDMS masses, at constant thickness 10 μm and constant porosity of 60.7%. (f, g) Optical photographs showing top and cross-sectional views of PDMS lenses formed as in (g) for PDMS masses of 3.5 and 16 mg. (h) Picture of a test pattern containing lines of width ranging from 250 to 4 μm, captured through a free-standing PDMS lens with focal length 4.7 mm adhered to a Samsung S5 camera. Inset (red box) shows the same test pattern captured with the same smartphone but without the lens. (i) Same as in (d), with a 3x digital zoom applied to the Samsung S5

camera. Inset shows the greyscale intensity profile of the picture in (i), from which it is apparent that lines with width down to 4 μm can be resolved. Lens was formed on a PSi layer with porosity of 75% and thickness of 10 μm by dropping 10 mg of PDMS. Data in c) and d) are provided as average values of 6 and 3 replicates, respectively, with error bars representing one standard deviation. All the lens images were taken after thermal curing, which was performed with the lens facing upwards.

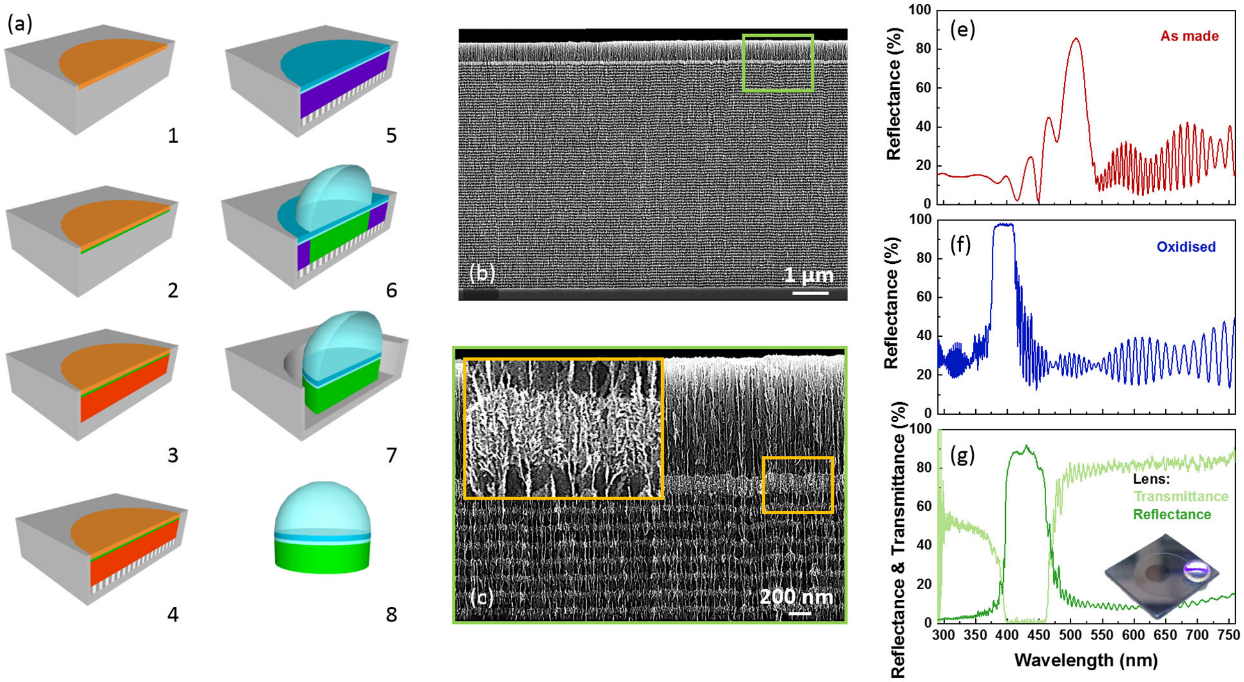

Figure 2. Preparation of free-standing PDMS lenses with embedded PSi UV-blue band-rejection filter.

(a) Key steps in the preparation of a PDMS lens with an embedded PSi optical filter component: 1- a high-porosity PSi templating layer (orange) is etched. This layer is designed to provide the correct surface interaction to direct the shape of the PDMS lens; 2- a low-porosity PSi barrier layer (green) is etched beneath the templating layer. This provides a barrier that minimizes infiltration of the liquid PDMS precursor into the subsequently etched optical filter layers; 3- the PSi optical filter component (red) is etched beneath the barrier layer; 4- a high-porosity release layer is etched beneath the optical filter; 5- the entire porous structure is thermally oxidized. The conditions are set such that all the porous layers convert to SiO_2, but the crystalline silicon substrate remains; 6- a drop of predetermined volume of the liquid PDMS pre-polymer material is deposited and thermally cured; 7- the silicon dioxide surrounding the PDMS lens and porous optical filter assembly is dissolved with a dilute aqueous HF solution; 8- the integral PDMS lens and optical filter component assembly is removed from the silicon chip. (b) SEM cross-section of the PSi stack showing the high-porosity templating layer (approx. 1 μm thick) on top, the low porosity barrier layer (approx. 100 nm thick), and the DBR structure consisting of 80 high-low porosity bi-layers. The brighter/darker regions correspond to the lower/higher porosity layers, respectively. (c) Higher magnification SEM image of the top portion of (b), from which the morphology of templating and barrier layers is more apparent. Inset shows a detail of the PSi barrier layer. (e, f) Reflectance spectrum of the PSi stack before thermal oxidation (step 4 of the fabrication procedure) (e) and after thermal oxidation (step 5 of the fabrication procedure) (f). (g) Reflectance and transmittance spectra of the free-standing PDMS lens embedding the PSi DBR (step 8 of the fabrication procedure). Inset shows a picture of the lens once removed from the silicon chip. The PDMS lens features a highly reflective violet color at the bottom due to the PSi DBR embedded in it.

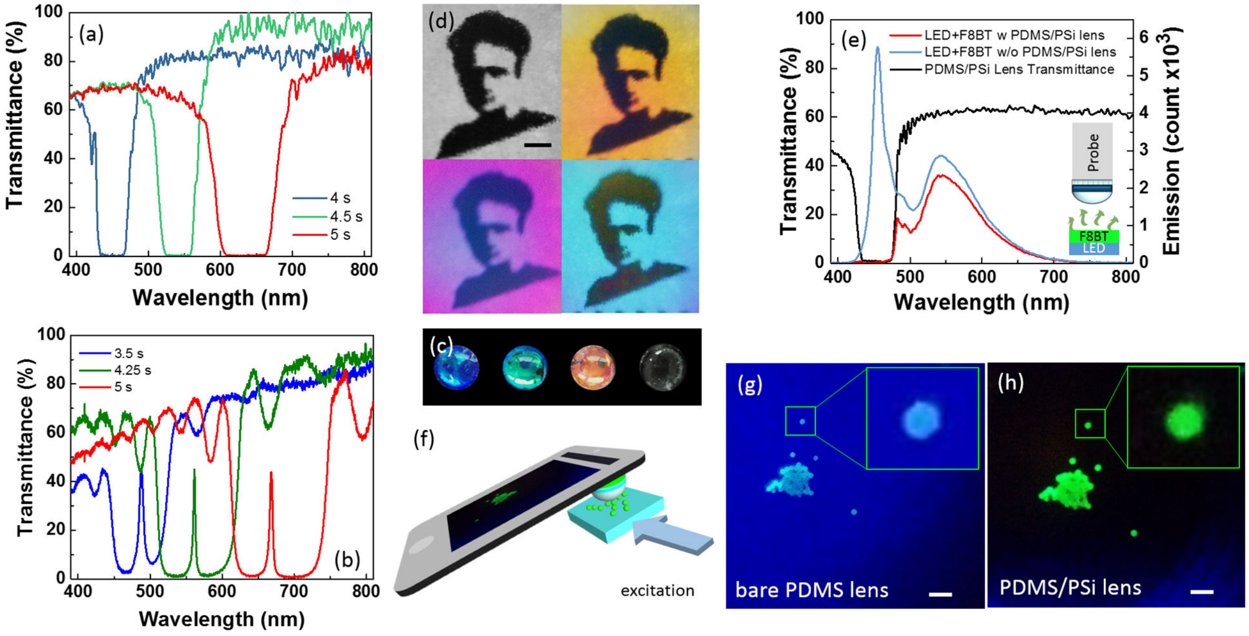

Figure 3. Optical microscopy with PDMS lenses containing integral PSi optical filter components.

(a) Transmittance spectra of three PDMS lenses with embedded PSi DBRs prepared with different visible wavelength pass-bands. (b) Transmission spectra of three PDMS lenses with embedded resonant cavities prepared with different cavity resonances from blue to red. Q-factor is 140. (c) Picture of the 3 PDMS/PSi lenses from (a) and a PDMS lens containing no optical filter, on black background. Lens diameter is approximately 4 mm. (d) Complementary-color pictures acquired on a greyscale Marie-Curie image using a smartphone Samsung S5 camera equipped with the PDMS/PSi lenses in (a), highlighting the simultaneous magnification and light filtering capabilities of the fabricated lenses. In particular: the use of the blue lens results in the yellow picture, red lens gives rise to the cyan picture, and the green lens gives rise to the magenta one. The greyscale picture was obtained with a plain PDMS lens (with similar focal length), without any PSi optical component. Marker is 1 mm. (e) Transmittance (black trace) spectrum of a blue-filtering PDMS/PSi lens superimposed on the emission spectrum of a blue LED coated with a green-emitting F8BT film, collected with a spectrometer probe without (blue trace) or fitted with the blue-filtering PDMS/PSi lens (red trace). (f) Conceptual sketch of a fluorescence microscope system (excitation band <450 nm, emission band > 500 nm) realized with a smartphone equipped with a blue-filtering PDMS/PSi lens. (g, h) Picture of fluorescent microbeads (approx. 60 μm in diameter) acquired with the setup sketched in (f) and blue laser excitation, using a plain PDMS lens (g) and a blue-filtering PDMS/PSi lens (h); insets in (g), (h) show a digital zoom of a single bead. Notice that the use of the blue-filtering PDMS/PSi lens in (g) effectively filters out the laser excitation light, rendering the green emission with high fidelity (marker is 150 μm). All the lens images were taken after thermal curing, which was performed with the lens facing upwards.

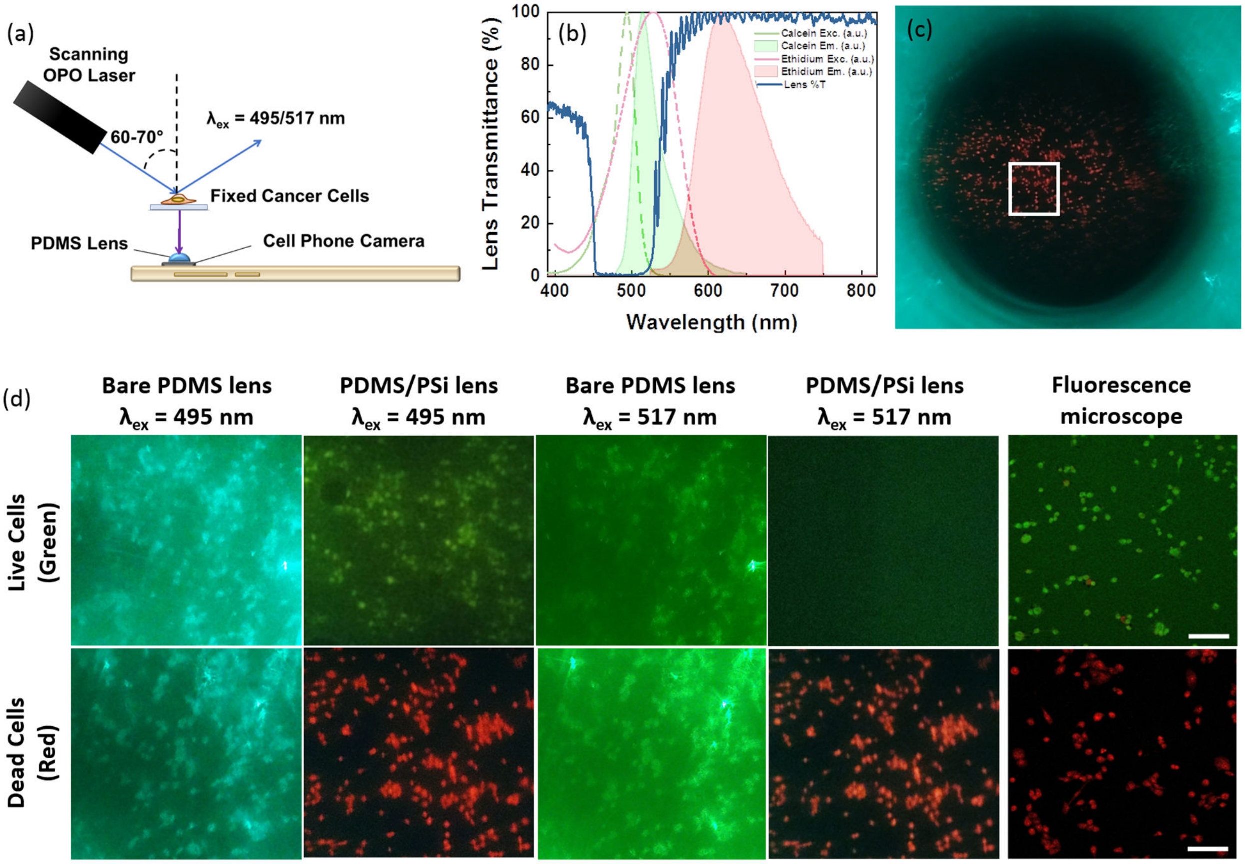

Figure 4. Imaging of mammalian cells with PDMS lenses containing an embedded PSi optical filter.

(a) Setup employed for imaging fixed CAOV-3 ovarian cancer cells that were stained with the live-dead assay reagents calcein AM and ethidium homodimer-1 (ThermoFisher L3224). Cells were fixed on glass coverslips, mounted on glass slides, placed on a 3-axis stage and illuminated with laser light at either 495 or 517 nm, as indicated. Focused cell images were collected with an AXON 7 (ZTE) cell phone camera (back) and remotely controlled with a computer. (b) Transmission spectrum of the PDMS-PSi lens employed for the fluorescent cell imaging, featuring a DBR with stop-band rejecting in the wavelength range 465–525 nm. Absorbance and emission spectra of calcein AM and ethidium homodimer-1 used for live and dead cell staining, respectively are also shown. (c) Image of dead cells acquired with smartphone equipped with the PDMS-PSi lens, upon excitation at 517 nm. The excitation light is effectively filtered out in the central area of the lens, enabling the red stained cells on a black background to be clearly imaged. (d) Representative live-dead cell images using a PDMS lens without (control lens) and with embedded PSi filter. Live (top row) or dead (bottom row) CAOV-3 ovarian cancer cells were prepared and treated with the calcein + ethidium staining solution and then fixed prior to imaging. Individual cells can be visualized at the magnification achieved with this PDMS lens. The PSi filter embedded in the PDMS lens effectively blocked the excitation light from entering the camera, such that only the fluorescence from the stained ovarian cancer cells was captured. The fluorescence reflects the live (green) or dead (red) state of the cells prior to fixation. Images collected with the control PDMS lens (without PSi filter) had high background luminescence and the cells strongly scattered the excitation light. Analagous fluorescence images obtained with a commercial, high-end (Zeiss LSM 710 NLO) confocal microscope ("Fluorescence microscope") are also reported for comparison. Marker is 200 μm and applies to all images in (d).

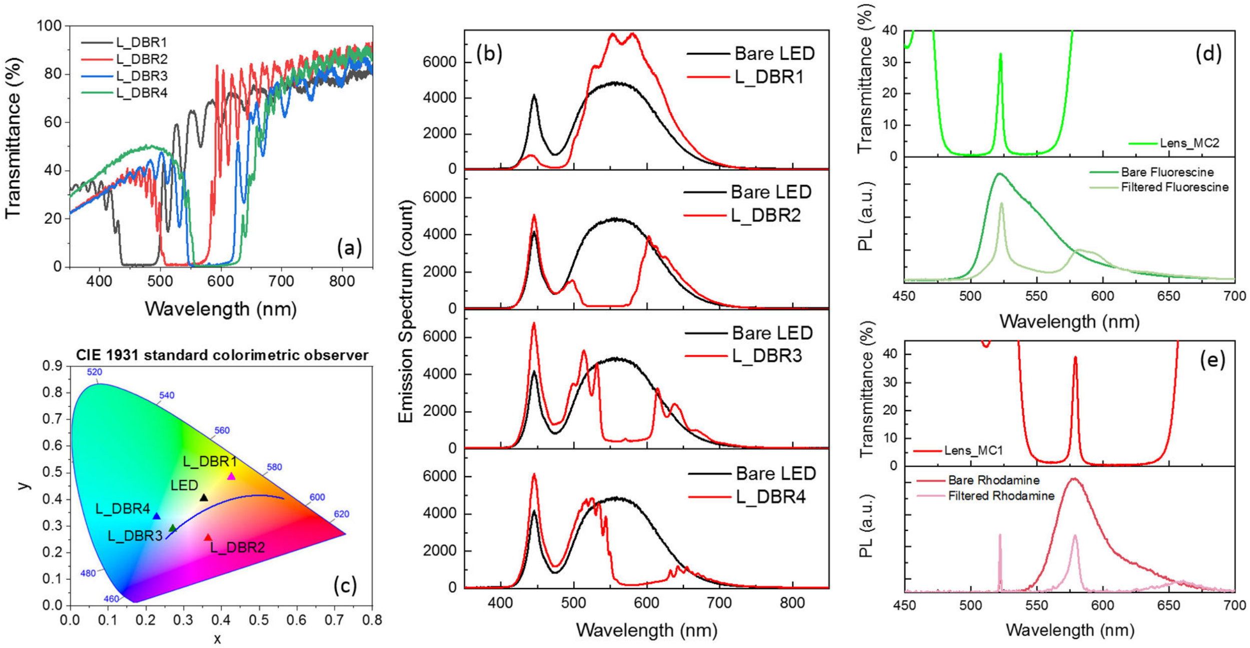

Figure 5. Spectra of white LED or molecular fluorophore light sources obtained through PDMS lenses that contained an embedded PSi optical filter, demonstrating shaping of the color spectrum and selection of specific, narrow wavelength bands.

(a) Transmission spectra obtained through composite PDMS/PSi lenses, where the stop-band of the porous silicon DBR filters were tuned to pre-determined regions of the visible spectrum. (b) Emission spectrum of a warm-white LED (black trace) superimposed on spectra of the same light source but collected through the PDMS/PSi lenses from (a), which were placed on top of the LED. The DBR embedded in the lens allowed the efficient removal of the LED light falling within the DBR stop-band. (c) Spectral data from (b) represented in a CIE 1931 diagram of the color perceived by the human eye. (d, e) Transmittance spectra of composite PDMS/PSi lenses that contained an embedded PSi microcavity whose resonant wavelength was engineered to fall within the emission spectrum of fluorescein (d) or rhodamine B (d). The fluorescence spectra of the two dyes were obtained without (“Bare Fluorescein” or “Bare Rhodamine”) or with (“Filtered Fluorescein” or “Filtered Rhodamine”) the lens applied to the collection probe of the spectrometer. The filtered spectra showed linewidth narrowing to 5 nm FWHM of the fluorescence from the dye.